



# Highly flexible transparent substrate-free photoanodes using ZnO nanowires on nickel microfibers

Hong Seok Jo<sup>a,1</sup>, Edmund Samuel<sup>a,1</sup>, Hyuk-Jin Kwon<sup>a</sup>, Bhavana Joshi<sup>b</sup>, Min-Woo Kim<sup>a</sup>,  
Tae-Gun Kim<sup>a</sup>, Mark T. Swihart<sup>c</sup>, Sam S. Yoon<sup>a,\*</sup>

<sup>a</sup> School of Mechanical Engineering, Korea University, Seoul 02841, Republic of Korea

<sup>b</sup> Department of Physics, NES Science College, Swami Ramanand Teerth Marathwada University, Latur Road, Nanded, Maharashtra 431606, India

<sup>c</sup> Department of Chemical & Biological Engineering, University at Buffalo, The State University of New York, Buffalo, NY 14260-4200, USA

## HIGHLIGHTS

- Breakthrough demonstration of freestanding flexible high-performance photoanodes.
- Uniform growth of ZnO nanowires improves photoelectrochemical performance.
- ZnO NW/Ni fiber photoanode produces photocurrent density of 1.14 mA/cm<sup>2</sup> at 0.4 V vs Ag/AgCl.
- Unique morphology provides exceptional stability even after 1000 bending cycles.

## ARTICLE INFO

### Keywords:

ZnO  
Nanowires  
Nickel  
Microfibers  
Flexible  
Transparent  
Substrate-free  
Photoanode

## ABSTRACT

We demonstrate impressive performance of photoanodes comprising ZnO nanowires grown over nickel fibers for efficient water splitting. The photoanode is substrate-free and flexible, exhibiting excellent stability (~98%) in photocurrent density even after 1000 bending cycles. The hierarchically structured ZnO nanowires on nickel microfibers synergistically provide many accessible electrochemical sites and enhance the photocurrent density to 1.14 mA/cm<sup>2</sup> at a voltage of 0.4 V vs. Ag/AgCl. The one- and two-dimensional structures of the ZnO nanowires over nickel microfibers enable an efficient charge-transport mechanism that supports high light-harvesting efficiency. Scanning and transmission electron microscopy are used to study the morphologies of the samples in detail, while X-ray diffraction confirms the metallic state of Ni and the crystallinity of ZnO.

## 1. Introduction

The direct utilization of solar energy for water splitting to produce clean energy is attracting significant attention [1–3]. Substrate- and binder-free flexible photoelectrodes are desirable in devices including solar cells [4], sensors [5], and energy storage devices [6]. The advantages of flexible and freestanding electrodes include decreased mass, increased bendability [7] in accordance with the applied device packaging, lack of unwanted binders, and avoidance of strain from lattice mismatches with the substrate [8–10]. Binder-free photoanodes can provide enhanced active-material loading and density, thus facilitating mass transport and improving light management by the photoanode material [11]. Electron-hole separation, fast charge transfer, broad-spectrum light absorption, and shallow photon penetration

allowing holes to reach the surface rapidly without bulk recombination are necessary physicochemical properties for excellent photoelectrochemical (PEC) performance.

Recently, metal oxides including Ti, Ni, W, Sn, FeCoW, and WO<sub>3</sub> have received substantial attention for use in photoanodes [12–15]. Song et al. reported WO<sub>3</sub> nanobelts that exhibited a photocurrent density (PCD) of 311 μA/cm<sup>2</sup> [16], Zely et al. demonstrated TiO<sub>2</sub> nanotubes achieving a PCD of 175 μA/cm<sup>2</sup> at 0.5 V [17], Kim et al. fabricated nanotextured β-Bi<sub>2</sub>O<sub>3</sub> pillars that produced the PCD of 1 mA/cm<sup>2</sup> [18], and Xiao et al. synthesized FeCoW/Fe<sub>2</sub>O<sub>3</sub> nanowires (NWs) by a sol-gel technique that showed the PCD of 1.18 mA/cm<sup>2</sup> at 1.23 V [14]. Although many metal oxides are promising for PEC water splitting, they generally suffer from surface oxidation and poor hole-transfer efficiency [19].

\* Corresponding author.

E-mail address: [skymoon@korea.ac.kr](mailto:skymoon@korea.ac.kr) (S.S. Yoon).

<sup>1</sup> These authors have contributed equally.

To address these challenges, photoanodes based upon nanoheterostructures such as NWs or nanorods with cocatalyst supports (such as Ni) have been developed. The hierarchical structuring of functional oxides can enhance PEC performance by facilitating charge separation. However, using a Ni cocatalyst as an underlayer allows fast charge transfer that may increase the electron-hole recombination rate. Therefore, decreasing the loading of Ni can be desirable. Thus, the growth of metal oxide nanostructures over Ni fibers, which produces a much higher metal oxide surface area compared to the Ni/metal oxide interfacial area, rather than using a two-dimensional planar geometry with equal interfacial areas, is a reasonable solution to suppress electron-hole recombination while providing the benefits of a heterostructure.

ZnO is a desirable candidate for water-splitting cells because it is abundant, low-cost, environmentally friendly, and high in quantum efficiency. ZnO is also a good photocatalyst [19–21] and cost-effective for PEC water splitting [22]. However, the PEC performance of ZnO is limited by its high recombination rate. The suppression of rapid recombination is possible by transforming the morphology of ZnO into nanorods, nanotubes, NWs, nanopropellers, and nanoribbons [23,24]. Liu et al. suggested the use of a cocatalyst as an electron acceptor layer along with one-dimensional (1D) ZnO for efficient photogenerated electron-hole separation [23]. The characteristic properties of different ZnO nanostructures provide the potential for various applications. Numerous methods have been reported for the growth of ZnO nanostructures; among them, seeded chemical bath deposition (s-CBD) involves neither vacuum equipment nor other complex instruments. The only requirement of s-CBD is the deposition of a ZnO seed layer before the growth of nanostructures [25,26].

Here we demonstrate a hierarchical design of a Ni microfiber as the underlayer with ZnO NWs as a shell. The Ni fiber (Ni F) increases electron transfer, while the ZnO NWs increase light absorbance, which promotes electron-hole generation and thus improves the PEC performance for water splitting. Additionally, the good photoactivity, suitable energy bandgap, and photochemical stability of the ZnO NWs are desirable properties. This article reports a substrate-free and flexible photoanode, detailed processing parameters, and a complete study supporting the optimal fabrication conditions for obtaining excellent physicochemical properties promoting the PEC performance of photoanodes for storing solar energy in chemical form through PEC water splitting.

## 2. Experimental procedures

### 2.1. Materials

The solution for electrospinning of polymer nanofibers was prepared by dissolving 8 wt% polyacrylonitrile (PAN,  $M_w = 150$  kDa, Sigma-Aldrich, USA) in *N,N*-dimethylformamide (DMF, 99.8%, Sigma-Aldrich, USA) by stirring for one day at 25 °C. The Ni electroplating solution comprised  $H_3BO_3$  (6 g, Sigma-Aldrich, USA), Ni  $(SO_3NH_2)_2 \cdot 4H_2O$  (80 g, Sigma-Aldrich, USA), and deionized (DI) water (200 mL); 1 M NaOH (Sigma-Aldrich, USA) was added dropwise to adjust the solution pH to 4.5. A 5-mM ZnO seeding solution of zinc acetate dihydrate (ZnAC,  $Zn(CH_3COO)_2 \cdot 2H_2O$ ,  $M_w = 219.51$ , Sigma-Aldrich, USA) was blended with propylene glycol for deposition on the surface of indium tin oxide (ITO) and Ni F by electrospinning. To prepare the precursor for ZnO NW growth, 0.1 mM ZnAC and 0.1 mM hexamethylenetetramine (HMT,  $C_6H_{12}N_4$ ,  $M_w = 140.19$ , Sigma-Aldrich, USA) were mixed in DI water and stirred for one day at room temperature of 25 °C [27].

### 2.2. Film fabrication

The fabrication process of the flexible electrode with Ni Fs is illustrated in Fig. 1a (upper schematic) as follows: first, the prepared PAN

solution is electrospun onto a square Cu frame ( $2.5 \times 1.5$  cm<sup>2</sup>) for different electrospinning times ( $t_{es}$ ) of 10, 30, 60, and 90 s. The flow rate is maintained at 200  $\mu$ L/h using a syringe pump (Legato 100, KD Scientific) and a needle (25-gauge, EFD). A Taylor cone is formed using a direct-current (DC) high-voltage power supply (EL20P2, Glassman High Voltage) that maintains a potential of 5.5 kV at the tip of the needle. The distance between the needle and the collector is 13 cm. In the second step, Pt is sputter-coated (Vacuum Device Inc., MSP-1S) for 2.5 s over the PAN nanofibers to provide sufficient conductivity for Ni electroplating. Next, the Pt-deposited PAN nanofibers (PAN NFs) are immersed in the Ni-plating solution and electroplated at 6 V using a DC power supply (E3642A 50 W power supply, Agilent, USA) for electroplating times ( $t_{ep}$ ) of 15, 30, 40, and 50 s, respectively, for the fiber mats with varying  $t_{es}$ , to produce similar Ni F diameters for all cases. Finally, the mat of Ni Fs is transferred onto a glass substrate and dried with  $N_2$  [28].

The bottom schematic of Fig. 1a illustrates the fabrication of ZnO NWs on the Ni Fs. The process steps progress as follows: first, the prepared ZnO seeding solution is sprayed onto the Ni Fs by electro-spraying for deposition times of  $t_s = 2, 5, 10,$  and 20 min. The solution is supplied to the needle at a flow rate of 0.08 mL/h via a syringe pump (Legato 100, KD Scientific) and 15 kV potential is applied to the nozzle (with 3-mm inner diameter) using a DC high voltage power supply (EL20P2, Glassman High Voltage). The sample is held 5 cm from the tip of the nozzle. Secondly, the ZnO seeded Ni Fs are annealed at 350 °C for 30 min and cooled at ambient temperature. After ZnO seeding on the Ni Fs, they are immersed in the prepared ZnAC/HMT solution for NW growth for different soaking times of  $t_g = 1, 1.5, 3,$  and 5 h. Finally, the ZnO NW-grown Ni Fs are dried at ambient temperature. Fig. 1b shows a transparent flexible conducting film comprising Ni Fs decorated with ZnO NWs. Attachment of the film to human skin is also demonstrated. The scanning electron microscopy (SEM, S-5000, Hitachi, Japan) and transmission electron microscopy (TEM, JEM 2100F, JEOL Inc., USA) images (Fig. 1c and d) show the uniformly distributed ZnO NWs on a Ni F. The ZnO seeding and ZnO NW formation were also performed on ITO substrates for the same spraying and growth times. The ITO substrate-based ZnO was used to study the effect of the change of substrate from ITO to Ni F on the PCD.

### 2.3. PEC characterization

The PCDs of ITO/ZnO NW and Ni F/ZnO NW working electrodes were measured in a three-electrode setup using a potentiostat (VersaSTAT-3, Princeton Applied Research, USA). A scan rate of 10 mV/s was used for PCD measurement over a voltage window of  $-0.4$  to  $0.4$  V, using an Ag/AgCl reference electrode and Pt wire counter electrode. The area of the working electrode immersed in the 0.5-M aqueous  $Na_2SO_4$  electrolyte of pH 6.8 was  $1 \times 1$  cm. Artificial sunlight generated by a Xe arc lamp with an AM 1.5 filter (Newport Oriel Instruments, USA) was used to illuminate the surface of the working electrode. The light intensity was adjusted to 100 mW/cm<sup>2</sup> using an optical sensor (918D-UV-OD3R, Newport Oriel Instruments, USA) and a light power meter (1919-R, Newport Oriel Instruments, USA). We maintained a fixed distance of 7 cm between the working electrode and lamp.

Electrochemical impedance spectroscopy (EIS) and Mott–Schottky plots were produced using the same PCD measuring equipment under 100 mW/cm<sup>2</sup> illumination. The frequency range of EIS measurement was 100 kHz to 0.1 Hz with a perturbation voltage of 10 mV. For the Mott–Schottky plots, the applied voltage range was  $-0.4$  to  $0.05$  V with a fixed frequency of 1000 Hz.

### 2.4. Characterization

SEM (SEM, S-5000, Hitachi, Japan) and a field-emission TEM (Tecnai G2 F30ST, Thermo Fisher Scientific, USA) with energy-

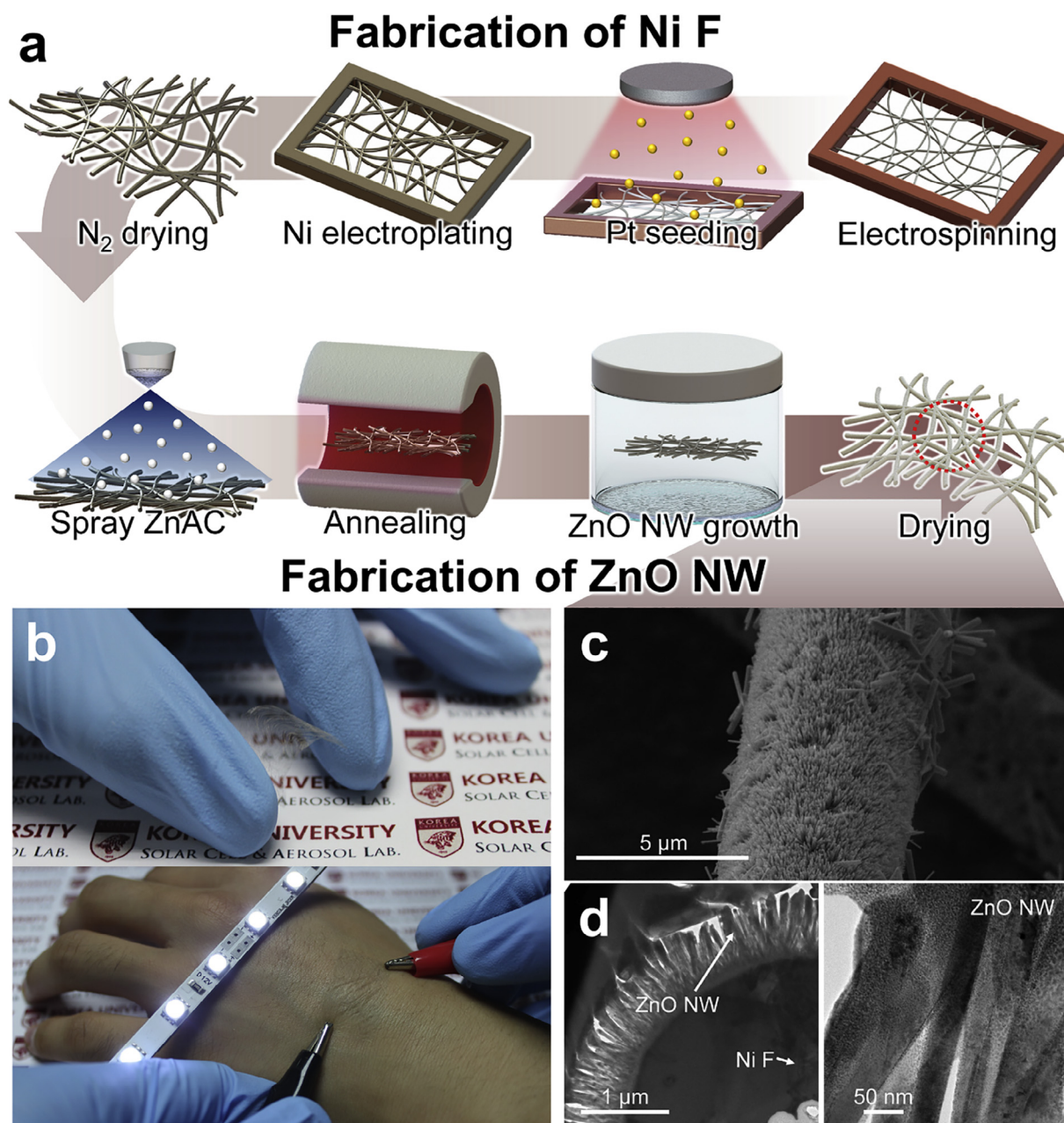


**Fig. 1.** (a) Schematic of the fabrication of Ni F and ZnO NW onto ITO or Ni F. (b) Flexible, bio-attachable, and transparent electrode with Ni Fs. (c) The top-view SEM and (d) cross-sectional TEM images of the ZnO NW-grown Ni Fs.

dispersive X-ray spectroscopy (EDS) were used to analyze the morphologies and elemental compositions of the Ni F/ZnO NW anodes. The phases of the ITO/ZnO NW and Ni F/ZnO NW specimens were determined by X-ray diffraction (XRD, SmartLab, Rigaku, USA), and the elemental compositions and chemical environments were characterized by X-ray photoelectron spectroscopy (XPS, X-TOOL, ULVAC-PHI, Inc., Japan). We measured the sheet resistance ( $R_s$ ) and transmittance ( $T$ ) of the Ni Fs using a sheet resistance meter (FPP-400, Dasol Eng, Republic of Korea) and an ultraviolet-visible (UV-VIS) spectrophotometer (Optizen POP, Mecasys, Republic of Korea), respectively. The lengths of the PAN NFs and diameters of the PAN NFs and Ni Fs were determined from SEM images using the imaging software I'MEASURE (I'MEASURE 2.0, ING PLUS, Republic of Korea).

### 3. Results and discussion

#### 3.1. Material characterization

The ZnO NWs were initially grown on ITO to optimize the growth process without the complication of a complex substrate (the Ni Fs). Two sets of experiments were completed. For the first case (I case\_ITO), ZnO NW growth used a fixed growth time ( $t_g$ ) and varying seeding time ( $t_s$ ), while for the second case (II case\_ITO),  $t_g$  was varied with fixed  $t_s$ . As mentioned in Section 1, we used s-CBD; therefore, observing the effects of varying  $t_s$  was important. The growth of NWs involves the decomposition of HMT to ammonia and formaldehyde. Thus, HMT works as a pH buffer. Further, in the presence of water, ammonia release yields both  $\text{NH}_4^+$  and  $\text{OH}^-$  ions. The  $\text{OH}^-$  reacts to form  $\text{Zn}(\text{OH})_2$  and then ZnO, as shown in Reaction (1) below. In the presence of the seed layer, ZnO NW growth occurs by heterogeneous nucleation at low

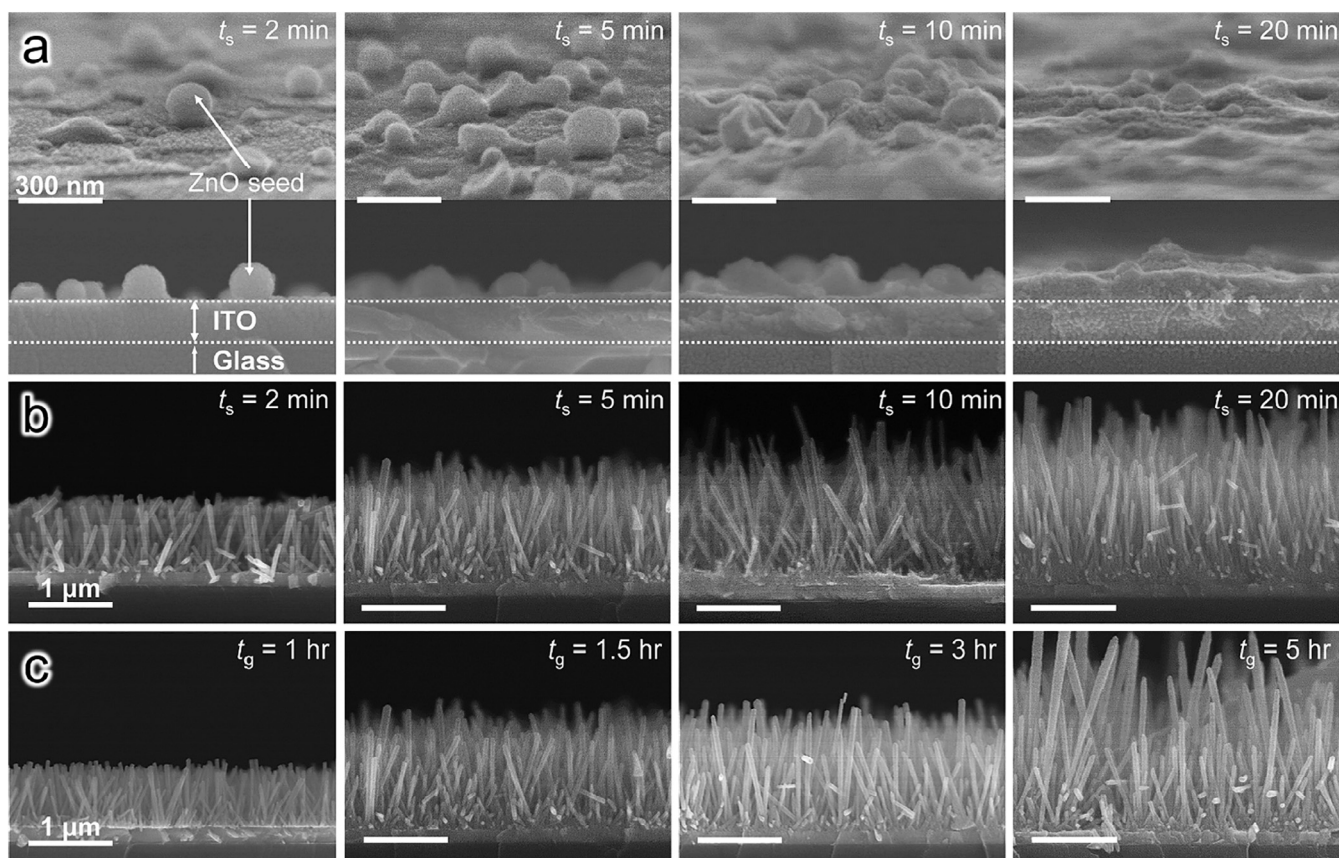


Fig. 2. (a) Tilted and side-view SEM images of the ZnO seed layer on ITO for  $t_s = 2, 5, 10,$  and  $20$  min. Side-view SEM images of the nano-textured ZnO NWs on ITO for (b)  $t_s = 2, 5, 10,$  and  $20$  min and (c)  $t_g = 1, 1.5, 3,$  and  $5$  h from left.

Table 1

Parameters of the PAN nanofiber and Ni F.

Parameter	PAN nanofiber			Ni fiber							
	$t_{es}$ [s]	$L_p$ [m]	$A_p$ [cm <sup>2</sup> ]	$t_{ep}$ [s]	$I$ [A]	$Q/A_p$ [C/cm <sup>2</sup> ]	$D_{Ni}$ [μm]	$\beta$	$T$ [%]	$R_s$ [Ω/sq]	
1	10	14.3	0.1123	15	2	267.1	3.1	0.359	92.3	1.45	
2	30	26.8	0.2104	28	2	266.1	3.1	0.673	78.5	0.460	
3	60	40.1	0.3149	40	2.1	266.7	3.12	1.01	61.2	0.197	
4	90	63.4	0.4979	55	2.4	265.1	3.1	1.59	49.1	0.099	

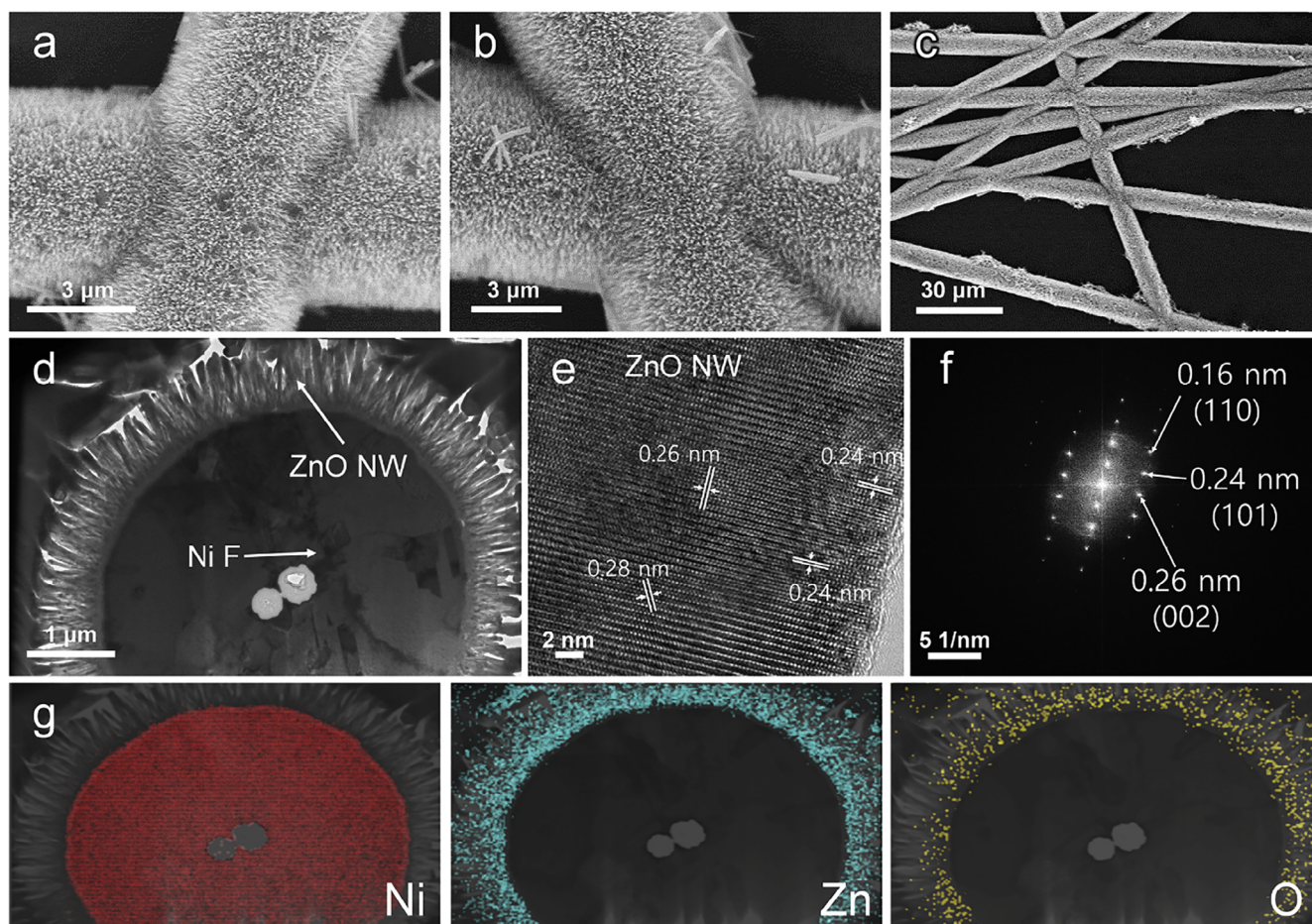
saturation levels of  $Zn(OH)_2$ , as shown in Reaction (2) [29].



Fig. 2a and b show the ZnO seed layer and ZnO NW growth of I case\_ITO at  $t_s = 2, 5, 10,$  and  $20$  min at the fixed  $t_g$  of  $1.5$  h. As shown in Fig. 2a, at  $t_s = 2$  min, the ZnO seeds of  $66$  nm in average diameter are deposited sparsely. As  $t_s$  is increased to  $10$  min, the deposition of ZnO seeds also increases on ITO. However, a thick ZnO seed layer does not form until  $t_s = 10$  min. At  $t_s = 20$  min, the ZnO seed layer has a thickness of  $202$  nm, because the higher  $t_s$  allows the ZnO seeds to fill empty spaces. As an effect of the ZnO seed layer  $t_s$  of  $2, 5, 10,$  and  $20$  min, the lengths of the ZnO NWs in s-CBD are  $0.79, 1.17, 1.77,$  and  $2.01$  μm, respectively, for  $t_g = 1.5$  h (see Fig. 2b). Furthermore, the ZnO NW growth of II case\_ITO for increasing  $t_g = 1, 1.5, 3,$  and  $5$  h at the fixed  $t_s = 5$  min is shown in Fig. 2c. At  $t_g = 1$  h, the length of the ZnO NW is the shortest ( $0.75$  μm) because of the small reaction time allowed for ZnO NW growth. With increasing  $t_g$ , the length of the ZnO NW is increased to  $1.17, 1.55,$  and  $2.17$  μm, while the ZnO NW diameters remain constant. In the electrochemical characterization described below,

the fabrication condition of  $t_s = 5$  min and  $t_g = 1.5$  h gave optimal performance, and therefore these conditions were used for ZnO seeding and NW growth for all of the tested Ni F/ZnO NW anodes.

In order to fabricate and demonstrate the use of the freestanding photoanode, Ni F deposition was studied first. The top-view SEM images in Fig. S1 show the Ni Fs formed for  $t_{es} = 10, 30, 60,$  and  $90$  s. As  $t_{es}$  was increased,  $t_{ep}$  was adjusted to maintain an approximately constant diameter of the Ni Fs ( $D_{Ni}$ ) for all cases.  $D_{Ni}$  is related to the quantity of electric charge ( $Q$ ) provided per unit area. The electroplating voltage and temperature of the electroplating solution were fixed at  $6$  V and  $30$  °C. As  $t_{es}$  increased, the current ( $I$ ) increased from  $2$  to  $2.4$  A because of the increased surface area for deposition ( $A_p = \pi D_p L_p$ , where  $D_p$  and  $L_p$  are the diameter and total length of the PAN nanofibers in the area of  $2.5 \times 1.5$  cm<sup>2</sup>, respectively) of the PAN nanofiber, as shown in Table 1. Because  $t_{ep}$  increases as  $t_{es}$  increases from  $10$  to  $30, 60,$  and  $90$  s,  $Q$  ( $Q = I t_{ep}$ ) is also increased from  $30$  to  $56, 84,$  and  $132$  C, respectively. However, the quantity of electric charge per unit area ( $Q/A_p$ ) is similar and near  $260$  C/cm<sup>2</sup> for all cases, as shown in Table 1. Therefore,  $D_{Ni}$  is approximately  $3$  μm for  $t_{es} = 10, 30, 60,$  and  $90$  s, as shown in Fig. S1a–d, respectively. As shown in Table 1, the



**Fig. 3.** Top-view SEM image of the nanotextured ZnO NW on Ni F at  $t_{\text{es}} = 60$  s: (a) Front and (b) rear high-magnification view. (c) Low-magnification ZnO NW/Ni F. (d) TEM image of the cross-sectional view of the Ni F/ZnO NW, (e) HRTEM image, (f) SAED pattern, and (g) elemental mapping of Ni, Zn, and O for Ni F/ZnO NW with  $t_{\text{es}} = 60$  s (Ni: red; Zn: cyan; O: yellow).

transmittance ( $T$ ) of the Ni F mat is decreased from 92.3 to 19.1% with increasing  $t_{\text{es}}$  and the sheet resistance ( $R_s$ ) is decreased from 1.45 to 0.099  $\Omega/\text{sq}$  because of the increased number of Ni Fs. The 3D network of conductive Ni Fs provides improved charge transfer and acceptor density compared to the ITO substrate.

The ZnO NWs are grown on the entire surface of the Ni F, as shown in Fig. 3a and b of the front and rear Ni F/ZnO NW, respectively, as the ZnO seeds are deposited on all Ni F surfaces. Moreover, ZnO NWs are evenly grown on the Ni F as shown in Fig. 3c. The low-magnification TEM image in Fig. 3d shows the cross-section of a Ni F/ZnO NW structure, confirming the formation of the Ni core and ZnO NW shell. The ZnO NWs grow perpendicular to the Ni F surface to a length of 1.17  $\mu\text{m}$ , approximately equal to that of the ITO/ZnO NW for  $t_s = 5$  min and  $t_g = 1.5$  h shown in Fig. 2b and c. The high-resolution TEM (HRTEM) image of the ZnO NW in Fig. 3e shows three different lattice spacings of 0.24, 0.26, and 0.28 nm, corresponding to the (1 0 1), (0 0 2), and (1 0 0) planes of ZnO. The selected-area electron diffraction (SAED) pattern in Fig. 3f exhibits the (1 0 1), (0 0 2), and (1 1 0) planes, where (1 1 0) has the lattice spacing of 0.16 nm; this is not observed in the HRTEM image because the spacing is too small to be distinguished. The ZnO NW planes in the SAED pattern match JCPDS card 80-0075. In elemental mapping (see Fig. 3g) of the Ni F/ZnO NW, the core and shell regions of the fiber show the presence of Ni and Zn, respectively. O is observed near Zn and at the interface of the Ni F and ZnO, forming a thin layer of NiO. Therefore, the elemental mapping confirms that the core region is mainly metallic Ni, which can rapidly capture electrons from the ZnO NW.

As shown in Fig. 4a, the crystalline phases of ITO and ZnO are

determined from the XRD patterns of the ITO/ZnO NW samples. The diffraction peaks of ITO are observed at  $2\theta$  values of 21.3, 30.2, 35.3, 45.4, 50.3, and 60.1°, corresponding to the (2 1 1), (2 2 2), (4 0 0), (4 3 1), (4 4 0), and (6 2 2) planes, respectively (JCPDS:71-2194); peaks of ZnO are found at 31.7, 34.3, and 36.2°, corresponding to the (1 0 0), (0 0 2), and (1 0 1) planes, respectively. Detailed analyses of the chemical composition and oxidation states of the Zn and Ni for ZnO NW grown over both ITO and Ni under optimal conditions were obtained by XPS characterization. The full XPS survey spectra for ITO/ZnO NW and Ni F/ZnO NW are shown in Fig. S2a and b, respectively. Furthermore, Fig. 4b and c depict the core XPS spectra in the Zn 2p and O 1s regions for the ITO/ZnO NW sample. As shown in Fig. 4b, the Zn 2p peaks, located at 1043.9 (Zn 2p<sub>1/2</sub>) and 1020.9 (Zn 2p<sub>3/2</sub>) eV, confirm the presence of Zn<sup>2+</sup> [30,31]. The O 1s core spectrum (Fig. 4c), when deconvoluted, shows three peaks at 529.6 eV (ZnO), 530.9 eV (Zn–OH), and 532.1 eV (C=O). The peak at 529.6 eV is attributed to Zn surrounded by O<sup>2-</sup> ions, while the binding energies of 530.9 eV and 532.1 eV correspond to oxygen-deficient states (O<sup>x-</sup> ( $x < 2$ )) from chemisorbed and dissociated O at the surface. The oxygen-deficient state of ZnO significantly benefits electron transport because it enhances the extrinsic semiconductive characteristics [32]. Fig. 4d shows the XRD pattern of Ni F/ZnO NWs. The distinctive peaks of ZnO (31, 35, and 36°) and Ni (44, 52, and 77°) are observed in Fig. 4d. The Ni peaks are much stronger, because of the relatively larger quantity and dimensions of Ni in the sample, compared to those of ZnO. The visible ZnO peaks correspond to the (1 0 1), (0 0 2), and (1 0 0) planes. Among these three planes of ZnO, the (1 0 1) plane is dominant, consistent with the HRTEM image (see Fig. 3e). The core XPS spectra of Ni and O of the

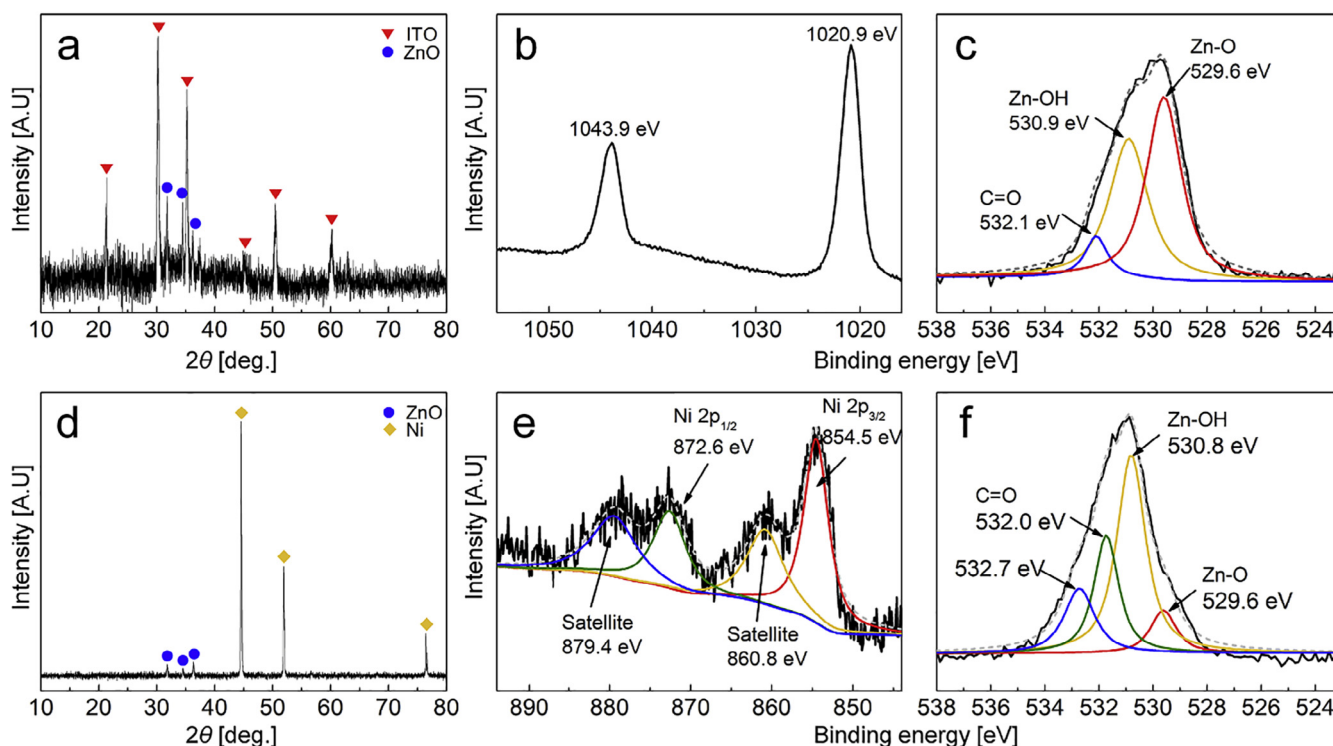


**Fig. 4.** The crystalline phases and composition analyses of ITO/ZnO NW and Ni F/ZnO NW: (a) XRD pattern, (b) Zn 2p core XPS spectrum, and (c) O 1s core XPS spectrum of ITO/ZnO NW. (d) XRD pattern, (e) Ni 2p core XPS spectrum, and (f) O 1s core XPS spectrum of Ni F/ZnO NW.

substrate-free Ni F/ZnO NW are presented in Fig. 4e and f, respectively. The Ni 2p<sub>1/2</sub> and Ni 2p<sub>3/2</sub> states yield peaks at 872.6 and 854.5 eV, respectively. The shake-up satellite peak at 879.4 eV is associated with Ni 2p<sub>1/2</sub>, while that at 860.8 eV indicates Ni 2p<sub>3/2</sub>, as shown in Fig. 4e. The satellite peaks appear at higher binding energies, which is consistent with previous reports [7]. Further, the deconvoluted O 1s core spectrum of Ni F/ZnO NW differs from that of ITO/ZnO NW because of the surface chemical composition over which the ZnO NWs were grown to form the hierarchical morphology. The three peaks at 529.6, 530.8, and 532 eV correspond to ZnO, ZnOH, and C=O; their features are similar to those explained earlier. However, the fourth deconvoluted peak at 532.7 eV indicates bonding at the interface of the ZnO NWs and Ni Fs [33].

### 3.2. PEC performance of ITO/ZnO NW

Absorbance of light by the photoanode produces photoexcited charge carriers, and may lead to charge separation. However, to achieve a high PCD for water splitting, the optimized thickness of the active-material layer is critical. Hence, the effect of  $t_s$  (I case\_ITO), corresponding to the various thicknesses of the ZnO seed layers, on the PCD was studied; the PEC performance is presented in Fig. 5a for anodes using a NW growth time ( $t_g$ ) of 1.5 h. For  $t_s = 2$  to 5 min, the peak PCD value is increased from 0.55 to 0.72 mA/cm<sup>2</sup> at a voltage of 0.4 V vs. Ag/AgCl, thus, the highest PCD of 0.72 mA/cm<sup>2</sup> is obtained for  $t_s = 5$  min at 0.4 V vs. Ag/AgCl. However, the PCD values for  $t_s$  of 10 and 20 min are decreased to 0.47 and 0.39 mA/cm<sup>2</sup> at a voltage of 0.4 V vs. Ag/AgCl, below the value at  $t_s = 2$  min, despite the increased layer thickness and ZnO NW length. As  $t_s$  increases from 2 to 20 min, the ZnO seed deposition is increased in density and the ZnO NW length is increased (see Fig. 2a and b). Therefore, the color of the sample ( $t_s \sim 20$  min) gradually whitens in the photograph in Fig. 5a. This suggests that the increased NW length increases the charge transport distance and density at higher  $t_s$ , ultimately decreasing the electric field and electron transfer rate and permitting more electron-hole

recombination.

EIS was performed under 1 sun illumination of 100 mW/cm<sup>2</sup>. The impedance ( $Z$ ) depends on the time ( $t$ ) and frequency ( $\omega$ ) as follows:

$$Z(\omega) = \frac{E_0 e^{j\omega t}}{I_0 e^{j(\omega t - \theta)}} = Z_0(\cos \theta - j \sin \theta) \quad (3)$$

where  $E_0$  and  $I_0$  are the initial potential and current, respectively. The components  $Z_0 \cos \theta$  and  $Z_0 \sin \theta$  are employed in analyzing the electrochemical performance of the active material. The plot of  $Z_0 \sin \theta$  (imaginary part) as a function of  $Z_0 \cos \theta$  (real part) is known as the Nyquist plot, which provides insights into the resistances in the overall electrochemical process.

Therefore, to clarify the resistances appearing during the electrochemical process, EIS analysis was performed for different samples of I case\_ITO and II case\_ITO. The values of solution resistance ( $R_{sol}$ ), resistance at the Helmholtz layer ( $R_H$ ), and electrode/electrolyte interface capacitance ( $C_H$ ) for ZnO NW on ITO are shown in Table 2. These electrical elements are useful to calculate the recombination lifetime ( $\tau_n$ ) at the interface of ZnO NW and the electrolyte from the following equation [34,35]:

$$\tau_n = R_H \times C_H \quad (4)$$

Fig. 5b shows the Nyquist plot of I case\_ITO; the impedance data are fitted with the equivalent electrical circuit presented in Fig. S3a.  $R_{sol}$  is slightly increased from 26.0 to 29.0  $\Omega$  with increasing seeding layer thickness, corresponding to the electrospinning time ( $t_s$ ), as shown in Table 2. The  $R_H$  and  $C_H$  from the Helmholtz layer at the interface between the ZnO NW electrode and electrolyte are utilized to calculate  $\tau_n$ . The value of  $C_H$  is the highest with a capacitance of  $75.7 \times 10^{-5}$  F when  $t_s = 2$  min; it is gradually decreased to 19.7, 7.90, and  $3.45 \times 10^{-5}$  F as  $t_s$  is increased from 5 to 20 min, respectively. The deduced recombination lifetime ( $\tau_n = 7.37 \times 10^{-2}$  s at  $t_s = 5$  min) provides sufficient charge separation time, which is consistent with the enhanced PCD value (see Fig. 5a) because it shows the smallest arc radius and the most efficient carrier transport. However, for the other cases,  $\tau_n$  is relatively lower, possibly because of the thin Helmholtz and

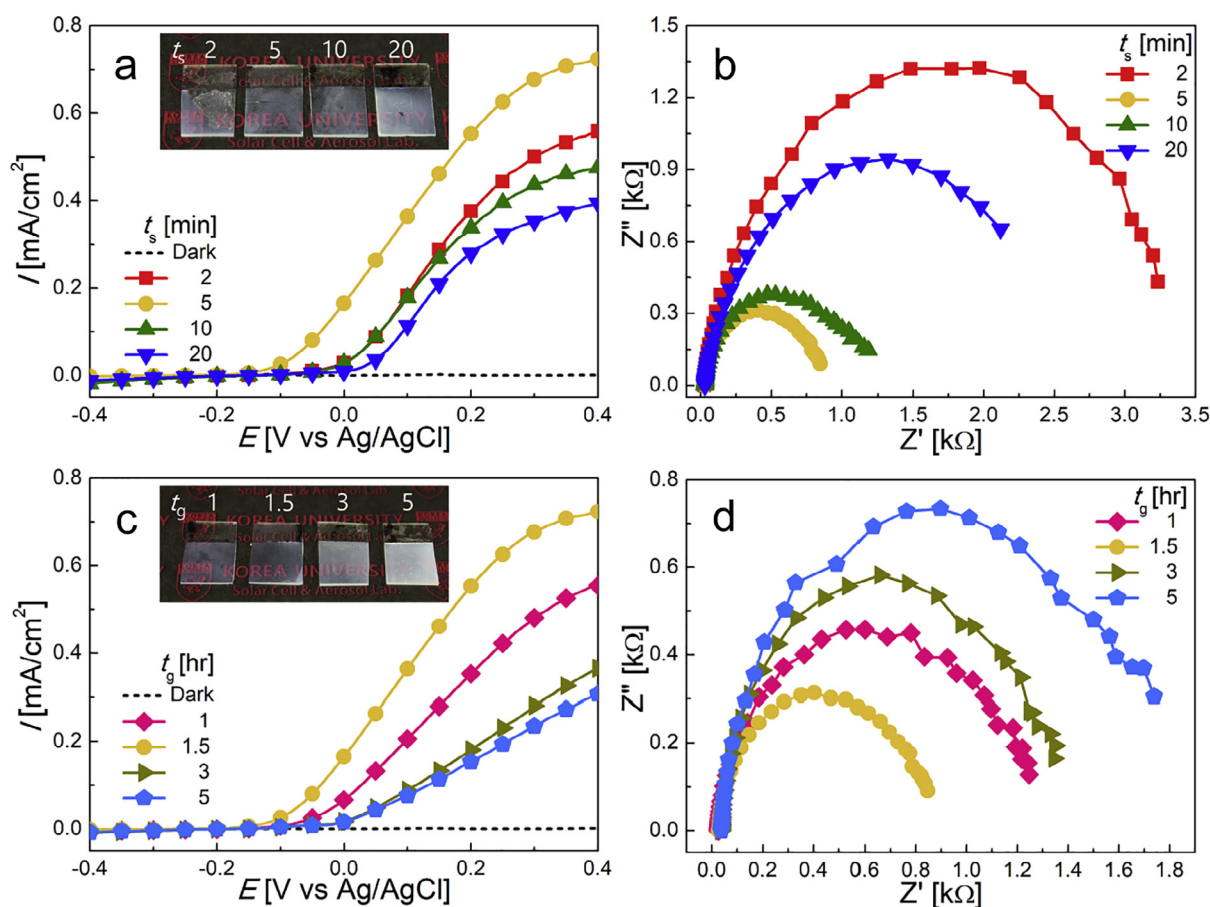


Fig. 5. PCD (a, c) and EIS (b, d) data for ITO/ZnO NW: (a) and (b) with varying  $t_s$  and (c) and (d) with varying  $t_g$ .

depletion layer formation, which consequently lowers  $R_{Hf}$  and  $C_H$  at the interface of ZnO NW and electrolyte. Additionally, a lower capacitance and resistance appears at the thin Helmholtz layer, which enable faster electron-hole recombination at the electrode surface (see Fig. S3b).

For the complete optimization of ZnO NW growth over the ITO substrate, II case\_ITO was also studied for PEC performance. Fig. 5c shows the effect of  $t_g$  (II case\_ITO) on the length of the ZnO NW for fixed  $t_s$  (seeding layer width). With the increase in  $t_g$ , the length of the ZnO NW is increased to 0.75, 1.17, 1.55, and 2.17  $\mu\text{m}$  (see Fig. 2c) and the deposited layer becomes whiter in the photograph in Fig. 5c. As shown in Fig. 5c, the PCD values at  $t_g = 1$  and 1.5 h are 0.55 and 0.72  $\text{mA}/\text{cm}^2$  at a voltage of 0.4 V vs. Ag/AgCl, respectively, which are the highest. However, the PCD values for  $t_g$  of 3 and 5 h are decreased to 0.36 and 0.31  $\text{mA}/\text{cm}^2$  at a voltage of 0.4 V vs. Ag/AgCl. Similar to I case\_ITO, the greater ZnO NW length limits the PCD performance. The reaction kinetics and  $\tau_n$  were analyzed via EIS to understand the efficient charge-separation and enhanced PCD values of the photoanode. The Nyquist plots for II case\_ITO are shown in Fig. 5d for different  $t_g$ . Here, ZnO NW grown over ITO is observed to replicate the morphology and height of NW obtained with I case\_ITO (see Fig. 2b and c). Thereby, the solution

resistances of the samples for both cases are as presented in Table 2. The resistance at the electrode/electrolyte interface, represented by  $R_{Hf}$ , for the optimal photoanode is higher (375  $\Omega$ ), and thus electron-hole recombination is slower and the enhanced PCD of 0.72  $\text{mA}/\text{cm}^2$  at a voltage of 0.4 V vs. Ag/AgCl is obtained.  $\tau_n$  is as shown in Fig. S3c. These results show that the solution resistance, Helmholtz resistance, and capacitance depend upon the photoanode morphology. Although the total number of reaction sites increases with the lengthening of the ZnO NWs,  $\tau_n$  shows a significant dependence on the resistance and capacitance generated at the electrode/electrolyte interface, such that longer ZnO NWs do not provide overall improved performance.

### 3.3. PEC performance of Ni F/ZnO NW

The optimized fabrication conditions for ZnO seeding and ZnO NW growth were  $t_s = 5$  min and  $t_g = 1.5$  h, as determined for ITO/ZnO NW. However, the PCD of the optimal morphology for ITO/ZnO NW remains limited by the fast surface recombination of electrons and holes and the limited exposure of ZnO NW for light absorbance. To overcome these limitations, ZnO NWs were grown over Ni F, providing enhanced light

Table 2

Parameters of the ITO/ZnO NW as I case\_ITO and II case\_ITO.

I case_ITO				II case_ITO			
$t_s$ [min]	$R_{sol}$ [ $\Omega$ ]	$R_{Hf}$ [ $\Omega$ ]	$C_H$ [ $10^{-5}$ F]	$t_g$ [hr]	$R_{sol}$ [ $\Omega$ ]	$R_{Hf}$ [ $\Omega$ ]	$C_H$ [ $10^{-5}$ F]
2	26.0	62.9	75.7	1	24.8	193	31.9
5	27.4	375	19.7	1.5	27.4	375	19.7
10	27.6	350	7.90	3	33.6	221	24.8
20	29.0	16.8	3.45	5	37.2	367	14.4

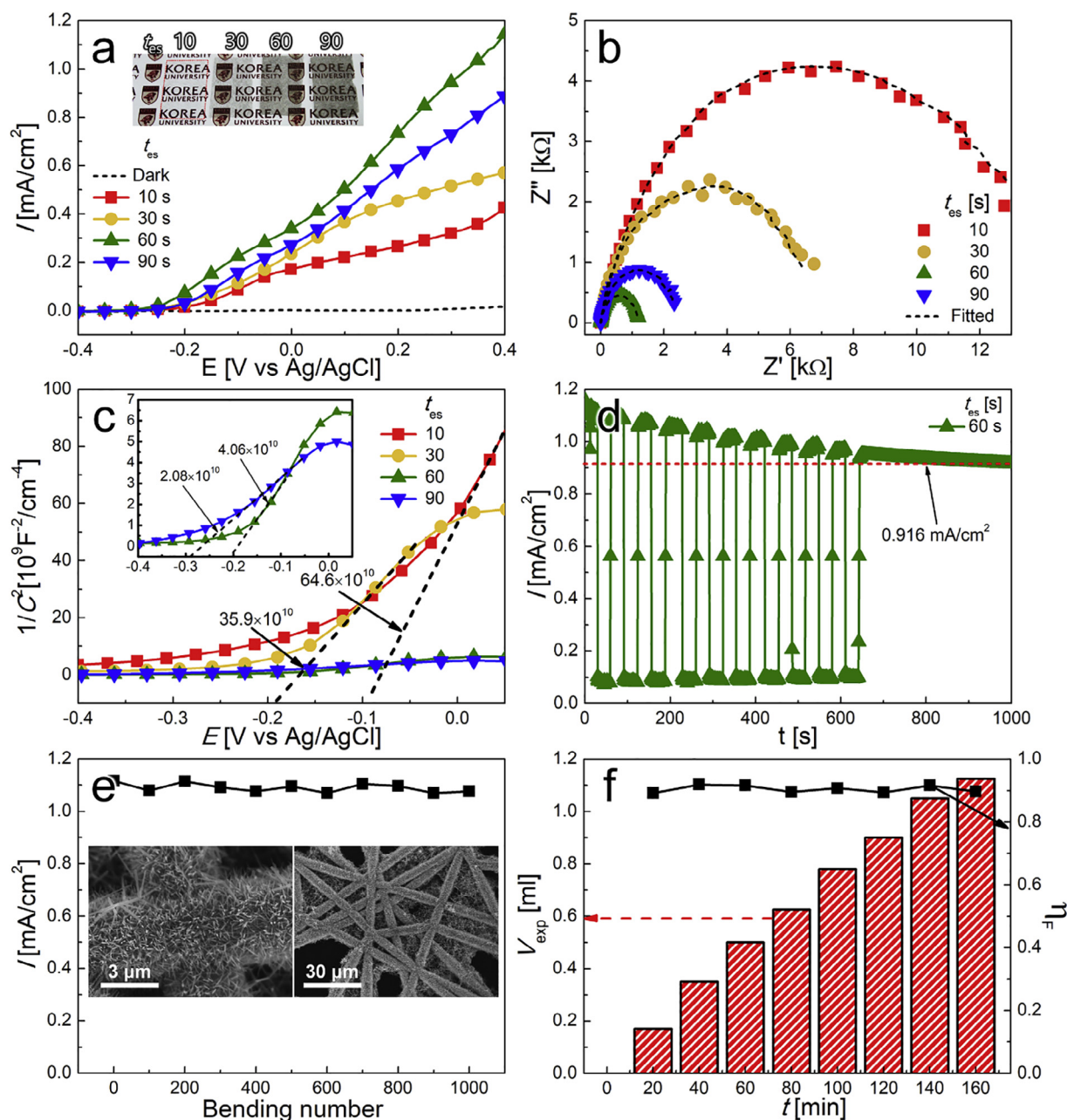


**Fig. 6.** Effect of the areal density of Ni F/ZnO NW on the PCD, with seeding ZnO on (a) both sides at  $t_{es} = 10, 30, 60,$  and  $90$  s. (b) Nyquist plots of EIS data measured under 1 sun illumination and (c) the Mott–Schottky curves obtained at 1000 Hz for varied  $t_{es}$ . (d) On–off testing, (e) bending test under 1 sun illumination with the inset SEM images showing Ni F/ZnO NW after 1000 bending cycles with  $t_{es} = 60$  s; (f)  $V_{exp}$  and  $\eta_F$  versus  $t$  from 0 to 160 min.

absorbance and a larger electrode/electrolyte interface (see Fig. 3d).

As shown in Fig. 6a, the PCD value at  $t_{es} = 60$  s is the highest, reaching  $1.14 \text{ mA/cm}^2$  at  $0.4 \text{ V}$ , although the amounts of Ni F and reaction areas continue to increase with increasing  $t_{es}$ . As the  $t_{es}$  is varied from 10 to 60 s, the ratio of the Ni F surface area ( $\beta$ ) is increased to 0.359, 0.673, and 1.01, as shown in Table 1, because of the increased number of Ni Fs. Moreover, the PCD value also increases to 0.43, 0.57, and  $1.14 \text{ mA/cm}^2$  at a voltage of  $0.4 \text{ V}$  vs. Ag/AgCl with increases in  $t_{es}$  up to 60 s. The photoanode with  $t_{es} = 60$  s exhibits a higher PCD than the samples with lower and higher  $t_{es}$  values. This enhanced PCD is mainly attributed to the dense array of ZnO NWs over the Ni F. The electron acceptor layer (Ni F) induces rapid electron transfer from the valence band to the conduction band under visible light in the optimal sample (see Fig. 6a). Moreover, the flexible Ni F/ZnO NW demonstrates an enhanced electrochemically active surface area (EASA), as deduced

using cyclic voltammetry as shown in Fig. S4. Table S1 shows a comparison of reported PCDs for similar anodes with those from the present study. Upon further increasing  $t_{es}$  to 90 s, the PCD value decreased to  $0.88 \text{ mA/cm}^2$  at a voltage of  $0.4 \text{ V}$  vs. Ag/AgCl, despite the increase in surface area ratio to 1.59. When  $t_{es}$  is low, the Ni F electrode has a single layer, and most of the incident light is absorbed by the ZnO NWs on the surfaces of the Ni Fs. Nevertheless, the PCD values at low  $t_{es}$  are also small because the number of Ni Fs is lower, yielding lower mass loading of the active material. In contrast, when  $t_{es}$  is too high, the electrode contains several layers of Ni Fs, and a step forms between the top and bottom layers of the Ni Fs, as shown in Fig. S1. Hence, the PCD value at high  $t_{es}$  could be decreased because the light transmitted from the top layer of ZnO NW is not absorbed sufficiently by the bottom Ni F layer because of its metallic nature, which is more reflective. The impact of Ni is also confirmed by diffuse reflectance spectra presented in

**Table 3**  
Parameters of the Ni F/ZnO NWs.

Ni F/ZnO NW							
Parameter	$t_{es}$ [s]	$R_{sol}$ [ $\Omega$ ]	$R_H$ [ $\Omega$ ]	$C_H$ [ $10^{-5}$ F]	$\tau_n$ [ $10^{-2}$ s]	$N_d$ [ $10^{19}$ cm $^{-3}$ ]	
1	10	5.44	206	0.585	0.12	0.151	
2	30	4.92	613	7.18	4.40	0.220	
3	60	3.83	342	7.40	2.53	1.08	
4	90	3.56	90.8	7.82	0.71	1.70	

**Fig. S5.** The PCD results according to  $t_{es}$  were also examined in detail through EIS and Mott–Schottky measurements.

**Fig. 6b** shows the EIS data for  $t_{es} = 10, 30, 60,$  and  $90$  s.  $R_{sol}$  decreases with increasing  $t_{es}$  from 10 to 90 s, as shown in **Table 3**. The decrease in resistance is because the Ni content and reaction area are increased as  $t_{es}$  is increased. The solution resistance and Helmholtz resistance for Ni F/ZnO NWs are obtained by fitting the Nyquist data. The equivalent circuit is shown in **Figure S3a**. The resistance at the electrolyte–Ni F/ZnO NW interface,  $R_H$ , also varies;  $R_H$  is obtained from fitting as 206, 613, 342, and 90.8  $\Omega$  for  $t_{es} = 10, 30, 60,$  and  $90$  s, respectively (see **Table 3**). Because  $R_H$  is higher at 613  $\Omega$  and  $C_H$  is  $7.40 \times 10^{-5}$  F when  $t_{es} = 30$  s,  $\tau_n$  of the electron-hole pair is higher, and therefore the photoanode achieves longer charge separation, thus enhancing the PEC performance in **Fig. S3d**.

Similar to  $\tau_n$ , donor concentration is also vital for the photoanode. The concentration of donors in the photoanode can be determined using the Mott–Schottky method, in which the charge capacitance ( $C$ ) is measured at 1000 Hz over the applied forward bias of  $-0.4$  to  $0.4$  V for the n-type semiconductor, using the Mott–Schottky equation [36,37]:

$$\frac{1}{C^2} = \frac{2}{\epsilon\epsilon_0 q A N_d} \left( E - E_{fb} - \frac{kT}{q} \right) \quad (5)$$

where the dielectric constant ( $\epsilon$ ) and the vacuum permittivity ( $\epsilon_0$ ) of ZnO are  $8.86 \times 10^{-14}$  and 8.5, respectively [38].  $q, A, N_d, E_{fb},$  and  $k$  are the electron charge ( $1.6 \times 10^{-19}$  C), electrode area, donor (electron) density (concentration), flat-band potential, and Boltzmann constant ( $1.38 \times 10^{-23}$  J K $^{-1}$ ), respectively. The slope of the Mott–Schottky plot at any point is positive for an n-type semiconductor because the bias becomes more positive with increasing electron density. In addition,  $N_d$  can be estimated from the slope of the plot, where the highest linear slope is denoted as  $\alpha$  [39–41].

$$\alpha = \frac{2}{\epsilon\epsilon_0 q A N_d} \Rightarrow N_d = \frac{2}{\epsilon\epsilon_0 q A \alpha} \quad (6)$$

The Mott–Schottky results in **Fig. 6c** show different tendencies from  $\tau_n$ . With increasing  $t_{es}$ ,  $\alpha$  is gradually decreased to 64.6, 35.9, 4.06, and  $2.08 \times 10^{10}$ , whereas  $N_d$  is increased to 0.151, 0.220, 1.08, and  $1.70 \times 10^{19}$  cm $^{-3}$  in **Fig. S3e**. The reaction area with the ZnO NW and electrolyte, related to  $\beta$  in **Table 1**, is increased because the amount of Ni Fs is also increased with increasing  $t_{es}$ . As the area is increased, more electrons are generated in the ZnO NW, and  $N_d$  is the highest at  $t_{es} = 90$  s. To compare the Ni F/ZnO NW and ITO/ZnO NW, the Mott–Schottky plot of the ITO/ZnO NW at  $t_s = 5$  min and  $t_g = 1.5$  h is presented as **Fig. S3f**. The donor concentration for ITO/ZnO NW at  $t_s = 5$  min and  $t_g = 1.5$  h is observed to be much smaller; hence, the PCD for the ITO/ZnO NW anode is low ( $N_d = 0.493 \times 10^{19}$  cm $^{-3}$ ). For  $t_{es} = 90$  s,  $N_d$  is much higher compared to all other cases. However, the large donor concentration decreases the thickness of the Helmholtz layer; therefore, rapid electron-hole recombination occurs. Consequently, the PEC performance suffers and lower PCD values are obtained. The donor concentration for Ni F/ZnO NW when  $t_{es}$  varies from 10 s to 90 s increases from  $\sim 0.2$  to  $1.7 \times 10^{19}$  cm $^{-3}$ . The flat-band potential decreases with increasing electrospinning time ( $t_{es} = 10$ – $90$  s), indicating the lowering of onset potential ( $-0.1$  to  $-0.29$  V) or the initiation of a photo-induced current at lower applied bias during PCD

measurements (see **Fig. 6a** and **c**). The flat-band potential almost coincides with the onset potential, as observed from linear-sweep voltammetry measurements.

On–off testing was performed as follows: the light illuminating the sample was blocked for 30 s, and then was shone for the same interval while the PCD was measured. This process was repeated 10 times; the light was then kept on for 350 s after cycling. As shown in **Fig. 6d**, the PCD graph is a step function, and the Ni F/ZnO NW immediately reacts to the light. Although the PCD value is initially 1.14 mA/cm $^2$  at a voltage of 0.4 V vs. Ag/AgCl, this value decreases with time; the PCD value after 1000 s is 0.916 mA/cm $^2$  at a voltage of 0.4 V vs. Ag/AgCl. The outstanding chemical and physical stability of the Ni F/ZnO NW is demonstrated in **Fig. 6e**. The Ni F/ZnO NW photoanode was bent 1000 times with a bending radius of 1 mm; at intervals of 100 bending cycles, we measured the PCD. The PCD data presented in **Fig. 6e** and the Ni F/ZnO NW bending radius ( $R_b$ ) of 0.3 cm is shown in **Fig. S6a**. The photoanode displayed the PCD retention of 1.14 mA/cm $^2$  at a voltage of 0.4 V vs. Ag/AgCl (98%) after 1000 bending cycles, compared to the initial PCD value of 1.15 mA/cm $^2$  at a voltage of 0.4 V vs. Ag/AgCl. The excellent physical stability of Ni F/ZnO NW arises from the highly flexible Ni F and good lattice matching of Ni and ZnO NW, which decreases the strain and stress in the anode. The high-magnification inset in **Fig. 6e** shows no signs of ZnO NW peeling off from the Ni F surfaces, while the low-magnification SEM image shows no Ni F damage or breakage.

The direct quantification of the Faradic efficiency ( $\eta_F$ ) of water splitting can be achieved by employing the ratio of the actual volume of produced hydrogen or oxygen ( $V_{actual}$ ) to the theoretical volume ( $V_{theo}$ ) that the current during PEC process can produce, as follows [42]:

$$\eta_F = \frac{V_{actual}}{V_{theo}} = \frac{V_{actual}}{(N_{H \text{ or } O} \cdot Q \cdot V_m) / (N \cdot F)} \quad (7)$$

where  $N_x$  is the moles of H $_2$  or O $_2$  per mole of H $_2$ O (for H $_2$ ,  $N_H = 2$ ; for O $_2$ ,  $N_O = 1$ ) and the total charge  $Q$  is the integrated current over time.  $V_m, N,$  and  $F$  are the molar volume of an ideal gas (22.4 L/mol at 293 K and 1 atm), the electrons per mole of H $_2$ O ( $N = 4$ ), and the Faraday constant ( $F = 96485$  C mol $^{-1}$ ), respectively. Although the working electrode of the Ni F/ZnO NW generates O $_2$  because of the n-type nature of ZnO, the amount of O $_2$  is so small that the volume change rate over time cannot be measured. Compared to O $_2$ , the volume of H $_2$  is visibly changed; therefore,  $\eta_F$  is calculated using H $_2$ . The PCD value and  $V_{actual}$  are measured for 160 min at the fixed potential of 0.4 V under 1 sun illumination.  $V_{actual}$  is gradually increased to 1.125 mL as  $t$  reaches 160 min (**Fig. 6f**), and the change of evolved gas volume is presented in **Fig. S6b**.  $\eta_F$ , obtained by Eq. (7), is maintained at  $\sim 90\%$  over a period of 160 min. The initial PCD value of 1.18 mA/cm $^2$  at a voltage of 0.4 V vs. Ag/AgCl shows 94% retention after 160 min, as shown in **Fig. S6c**. The inset shows the self-built H $_2$ /O $_2$  collector with measuring scale.

#### 4. Conclusion

We demonstrate a novel design of ZnO NWs over Ni Fs and the successful fabrication of a substrate-free and flexible photoanode with enhanced PEC performance. The hierarchical design enhances electron-hole separation and provides a short pathway for rapid electron

transfer. The PCD data shows that the PEC performance of the ZnO NW/Ni F is better than that of a ZnO NW/ITO. The PCD (1.14 mA/cm<sup>2</sup> at a voltage of 0.4 V vs. Ag/AgCl) of the ZnO NW/Ni F is 58% higher than that of the ZnO NW/ITO (~0.72 mA/cm<sup>2</sup> at a voltage of 0.4 V vs. Ag/AgCl). In addition, the onset potential for the former is significantly shifted negatively (> 0.1 V). The enhanced PEC properties of the ZnO NW/Ni F arise from the uniform growth of ZnO NW over the surfaces of the Ni Fs, as the photoanode is substrate-free. Thus, this work provides a new method for substrate-free photoelectrode design to promote PEC water-splitting performance toward the capture and storage of clean energy.

## Acknowledgements

This research was supported by the Technology Development Program to Solve Climate Changes of the National Research Foundation (NRF) of Korea funded by the Ministry of Science, ICT & Future Planning (NRF-2016M1A2A2936760), NRF-2017R1A2B4005639, and NRF-2013R1A5A1073861

## Appendix A. Supplementary data

Supplementary data to this article can be found online at <https://doi.org/10.1016/j.cej.2019.01.099>.

## References

- R. Zhang, F. Ning, S. Xu, L. Zhou, M. Shao, M. Wei, Oxygen vacancy engineering of WO<sub>3</sub> toward largely enhanced photoelectrochemical water splitting, *Electrochim. Acta* 274 (2018) 217–223.
- H. Han, S. Kment, F. Karlicky, L. Wang, A. Naldoni, P. Schmuki, R. Zboril, Sb-Doped SnO<sub>2</sub> nanorods underlayer effect to the  $\alpha$ -Fe<sub>2</sub>O<sub>3</sub> nanorods sheathed with TiO<sub>2</sub> for enhanced photoelectrochemical water splitting, *Small* 14 (2018) 1703860.
- F. Cao, W. Tian, L. Li, Ternary non-noble metal zinc-nickel-cobalt carbonate hydroxide cocatalysts toward highly efficient photoelectrochemical water splitting, *J. Mater. Sci. Technol.* 34 (2018) 899–904.
- Q. Cheng, D. Ye, W. Yang, S. Zhang, H. Chen, C. Chang, L. Zhang, construction of transparent cellulose-based nanocomposite papers and potential application in flexible solar cells, *ACS Sustain. Chem. Eng.* (2018).
- Y. Zhang, J. Xiao, Y. Sun, L. Wang, X. Dong, J. Ren, W. He, F. Xiao, Flexible nanohybrid microelectrode based on carbon fiber wrapped by gold nanoparticles decorated nitrogen doped carbon nanotube arrays: in situ electrochemical detection in live cancer cells, *Biosens. Bioelectron.* 100 (2018) 453–461.
- B.N. Joshi, S. An, Y.I. Kim, E.P. Samuel, K.Y. Song, I.W. Seong, S.S. Al-Deyab, M.T. Swihart, W.Y. Yoon, S.S. Yoon, Flexible freestanding Fe<sub>2</sub>O<sub>3</sub>-SnO<sub>x</sub>-carbon nanofiber composites for Li ion battery anodes, *J. Alloys Compd.* 700 (2017) 259–266.
- A. Sahasrabudhe, H. Dixit, R. Majee, S. Bhattacharyya, Value added transformation of ubiquitous substrates into highly efficient and flexible electrodes for water splitting, *Nat. Commun.* 9 (2018) 2014.
- J. Bandyopadhyay, K. Gupta, Low temperature lattice parameter of nickel and some nickel-cobalt alloys and grüneisen parameter of nickel, *Cryogenics* 17 (1977) 345–347.
- N. Nadaud, N. Lequeux, M. Nanot, J. Jove, T. Roisnel, Structural studies of tin-doped indium oxide (ITO) and In<sub>4</sub>Sn<sub>3</sub>O<sub>12</sub>, *J. Solid State Chem.* 135 (1998) 140–148.
- O. Madelung, U. Rössler, M. Schulz, II-VI and I-VII Compounds; Semimagnetic Compounds, Springer-Verlag, Berlin Heidelberg, 1999, pp. 1–5.
- N. Vogel, M. Retsch, C.-A. Fustin, A. del Campo, U. Jonas, Advances in colloidal assembly: the design of structure and hierarchy in two and three dimensions, *Chem. Rev.* 115 (2015) 6265–6311.
- L. Wang, Y. Wang, P. Schmuki, S. Kment, R. Zboril, Nanostar morphology of plasmonic particles strongly enhances photoelectrochemical water splitting of TiO<sub>2</sub> nanorods with superior incident photon-to-current conversion efficiency in visible/near-infrared region, *Electrochim. Acta* 260 (2018) 212–220.
- P. Wu, Z. Liu, D. Chen, M. Zhou, J. Wei, Flake-like NiO/WO<sub>3</sub> pn heterojunction photocathode for photoelectrochemical water splitting, *Appl. Surf. Sci.* 440 (2018) 1101–1106.
- J. Xiao, H. Huang, Q. Huang, X. Li, X. Hou, L. Zhao, R. Ma, H. Chen, Y. Li, Remarkable improvement of the turn-on characteristics of a Fe<sub>2</sub>O<sub>3</sub> photoanode for photoelectrochemical water splitting with coating a FeCoW oxy-hydroxide gel, *Appl. Catal. B* 212 (2017) 89–96.
- J. Zhang, Z. Liu, Z. Liu, Novel WO<sub>3</sub>/Sb<sub>2</sub>S<sub>3</sub> heterojunction photocatalyst based on WO<sub>3</sub> of different morphologies for enhanced efficiency in photoelectrochemical water splitting, *ACS Appl. Mater. Interfaces* 8 (2016) 9684–9691.
- K. Song, F. Gao, W. Yang, E. Wang, Z. Wang, H. Hou, WO<sub>3</sub> mesoporous nanobelts towards efficient photoelectrocatalysts for water splitting, *ChemElectroChem* 5 (2018) 322–327.
- M. Zelný, S. Kment, R. Ctvrtlík, S. Pausova, H. Kmentova, J. Tomastik, Z. Hubicka, Y. Rambabu, J. Krysa, A. Naldoni, TiO<sub>2</sub> Nanotubes on transparent substrates: control of film microstructure and photoelectrochemical water splitting performance, *Catalysts* 8 (2018) 25.
- M.-W. Kim, B. Joshi, E. Samuel, K. Kim, Y.-I. Kim, T.-G. Kim, M.T. Swihart, S.S. Yoon, Highly nanotextured  $\beta$ -Bi<sub>2</sub>O<sub>3</sub> pillars by electrostatic spray deposition as photoanodes for solar water splitting, *J. Alloys Compd.* (2018).
- S. Cao, X. Yan, Z. Kang, Q. Liang, X. Liao, Y. Zhang, Band alignment engineering for improved performance and stability of ZnFe<sub>2</sub>O<sub>4</sub> modified CdS/ZnO nanostructured photoanode for PEC water splitting, *Nano Energy* 24 (2016) 25–31.
- B.N. Joshi, H. Yoon, H.Y. Kim, J.H. Oh, T.Y. Seong, S.C. James, S.S. Yoon, Effect of zinc acetate concentration on structural, optical and electrical properties of ZnO thin films deposited by electrostatic spray on an ITO substrate, *J. Electrochem. Soc.* 159 (2012) H716–H721.
- Z. Zhang, Efficiency enhancement of ZnO/Cu<sub>2</sub>O solar cells with well oriented and micrometer grain sized Cu<sub>2</sub>O films, *Appl. Phys. Lett.* 112 (2018) 042106.
- S. Guo, X. Zhao, W. Zhang, W. Wang, Optimization of electrolyte to significantly improve photoelectrochemical water splitting performance of ZnO nanowire arrays, *Mater. Sci. Eng. B* 227 (2018) 129–135.
- Z. Liu, J. Zhang, W. Yan, Enhanced photoelectrochemical water splitting of photoelectrode simultaneously decorated with cocatalysts based on spatial charge separation and transfer, *ACS Sustain. Chem. Eng.* 6 (2018) 3565–3574.
- J. Han, Z. Liu, K. Guo, B. Wang, X. Zhang, T. Hong, High-efficiency photoelectrochemical electrodes based on ZnIn<sub>2</sub>S<sub>4</sub> sensitized ZnO nanotube arrays, *Appl. Catal. B* 163 (2015) 179–188.
- O. Farhat, M. Halim, N.M. Ahmed, M. Qaeed, ZnO nanofiber (NFs) growth from ZnO nanowires (NWs) by controlling growth temperature on flexible Teflon substrate by CBD technique for UV photodetector, *Superlattices Microstruct.* 100 (2016) 1120–1127.
- C.-H. Ku, H.-H. Yang, G.-R. Chen, J.-J. Wu, Wet-chemical route to ZnO nanowire-layered basic zinc acetate/ZnO nanoparticle composite film, *Cryst. Growth Des.* 8 (2007) 283–290.
- M.C. Akgun, Y.E. Kalay, H.E. Unalan, Hydrothermal zinc oxide nanowire growth using zinc acetate dihydrate salt, *J. Mater. Res.* 27 (2012) 1445–1451.
- H.-S. Jo, M.-W. Kim, B. Joshi, E. Samuel, H. Yoon, M.T. Swihart, S.S. Yoon, Ni-core CuO-shell fibers produced by electrospinning and electroplating as efficient photocathode materials for solar water splitting, *Nanoscale* 10 (2018) 9720–9728.
- C.P. Tsangarides, H. Ma, A. Nathan, ZnO nanowire array growth on precisely controlled patterns of inkjet-printed zinc acetate at low-temperatures, *Nanoscale* 8 (2016) 11760–11765.
- R. Al-Gaashani, S. Radiman, A. Daud, N. Tabet, Y. Al-Douri, XPS and optical studies of different morphologies of ZnO nanostructures prepared by microwave methods, *Ceram. Int.* 39 (2013) 2283–2292.
- D.R. Kumar, D. Manoj, J. Santhanalakshmi, Au–ZnO bullet-like heterodimer nanoparticles: synthesis and use for enhanced nonenzymatic electrochemical determination of glucose, *RSC Adv.* 4 (2014) 8943–8952.
- L. Liu, Z. Mei, A. Tang, A. Azarov, A. Kuznetsov, Q.-K. Xue, X. Du, Oxygen vacancies: The origin of n-type conductivity in ZnO, *Phys. Rev. B* 93 (2016) 235305.
- M.S. Abdel-Wahab, A. Jilani, I. Yahia, A.A. Al-Ghamdi, Enhanced the photocatalytic activity of Ni-doped ZnO thin films: Morphological, optical and XPS analysis, *Superlattices Microstruct.* 94 (2016) 108–118.
- Q. Wang, S. Ito, M. Grätzel, F. Fabregat-Santiago, I. Mora-Sero, J. Bisquert, T. Bessho, H. Imai, Characteristics of high efficiency dye-sensitized solar cells, *J. Phys. Chem. B* 110 (2006) 25210–25221.
- J. Bisquert, A. Zaban, M. Greenshtein, I. Mora-Seró, Determination of rate constants for charge transfer and the distribution of semiconductor and electrolyte electronic energy levels in dye-sensitized solar cells by open-circuit photovoltage decay method, *J. Am. Chem. Soc.* 126 (2004) 13550–13559.
- Y.J. Jang, J.-W. Jang, S.H. Choi, J.Y. Kim, J.H. Kim, D.H. Youn, W.Y. Kim, S. Han, J.S. Lee, Tree branch-shaped cupric oxide for highly effective photoelectrochemical water reduction, *Nanoscale* 7 (2015) 7624–7631.
- W. Gomes, D. Vanmaekelbergh, Impedance spectroscopy at semiconductor electrodes: review and recent developments, *Electrochim. Acta* 41 (1996) 967–973.
- L. Mentar, H. Lahmar, M.R. Khelladi, A. Azizi, The effect of bath temperature on the electrodeposition of zinc oxide nanostructures via nitrates solution, *J. New Technol. Mater.* 277 (2014) 1–5.
- K. Siuzdak, M. Szkoda, M. Sawczak, A. Lisowska-Oleksiak, J. Karczewski, J. Ryl, Enhanced photoelectrochemical and photocatalytic performance of iodine-doped titania nanotube arrays, *RSC Adv.* 5 (2015) 50379–50391.
- T. Karazehir, M. Ates, A.S. Sarac, Mott-Schottky and morphologic analysis of poly(pyrrrole-n-propionic acid) in various electrolyte systems, *Int. J. Electrochem. Sci.* 10 (2015) 6146–6163.
- S. Shen, J. Zhou, C.-L. Dong, Y. Hu, E.N. Tseng, P. Guo, L. Guo, S.S. Mao, Surface engineered doping of hematite nanorod arrays for improved photoelectrochemical water splitting, *Sci. Rep.* 4 (2014) 6627.
- S. Zhao, J. Huang, Y. Liu, J. Shen, H. Wang, X. Yang, Y. Zhu, C. Li, Multimetallic Ni–Mo/Cu nanowires as nonprecious and efficient full water splitting catalyst, *J. Mater. Chem. A* 5 (2017) 4207–4214.